Bucknell University
Bucknell Digital Commons

Faculty Journal Articles | Faculty Scholarship

9-2013

Integrated Geophysical Investigation of the St. James Fault Complex: A Case Study

Robert W. Jacob
Bucknell University, rwj003@bucknell.edu

Jeremy B. Byler

Mary Beth Gray
Bucknell University, mbgray@bucknell.edu

Follow this and additional works at: https://digitalcommons.bucknell.edu/fac_journ

 Part of the Geology Commons, and the Geophysics and Seismology Commons

Recommended Citation

Robert W. Jacob, Jeremy B. Byler, and Mary Beth Gray, (2013), "Integrated geophysical investigation of the St. James Fault Complex: A case study," GEOPHYSICS 78: B275-B285. https://doi.org/10.1190/geo2012-0426.1

This Article is brought to you for free and open access by the Faculty Scholarship at Bucknell Digital Commons. It has been accepted for inclusion in Faculty Journal Articles by an authorized administrator of Bucknell Digital Commons. For more information, please contact dcadmin@bucknell.edu.

Full Title

Integrated Geophysical Investigation of the St. James Fault Complex: a Case Study

Authors

Robert W. Jacob[1], rwj003@bucknell.edu

Jeremy B. Byler[2], jbyler@armgroup.net

Mary Beth Gray[1], mbgray@bucknell.edu

Affiliation

[1] Bucknell University, Lewisburg, PA USA

[2] ARM Group, Inc., Hershey, PA USA

Running Title:

Multi-method case study of St James Fault

Keywords:

Nippenose Valley PA, Nittany Anticlinorium, Very Low Frequency Electromagnetics, VLF, Electrical Resistivity, DC resistivity, Gravity, Micro-gravity, Bellefonte Formation, Valley and Ridge Province, Central Appalachians

Submission Record:

Manuscript submitted to Geophysics: 6 October 2012;

Revised manuscript submitted: 14 March 2013 and 19 June 2013

Manuscript accepted: 30 June 2013

Integrated Geophysical Investigation of the St. James Fault Complex: a Case Study

Robert W. Jacob, Jeremy B. Byler, and Mary Beth Gray

ABSTRACT

This case study non-invasively detects the characteristics and location of a regional fault in an area of poor bedrock exposure complicated by karst weathering features in the subsurface. Because this regional fault is associated with sinkhole formation, its location is important for hazard avoidance. The bedrock lithologies on either side of the fault trace are similar; hence we chose an approach that capitalized on the complementary strengths of very low frequency electromagnetic (VLF), resistivity, and gravity methods. VLF proved most useful as a first-order reconnaissance tool, allowing us to define a narrow target area for further geophysical exploration. Fault-related epikarst was delineated using resistivity. Ultimately, a high-resolution gravity survey and subsequent inverse modeling using results of resistivity survey helped to further constrain the location and approximate orientation of the fault. The combined results indicate that the location of the fault trace needs to be adjusted 53 m south of the current published location and is consistent with a north-dipping thrust fault. Additionally, a gravity low south of the fault trace agrees with the location of conductive material from the resistivity and VLF surveys. We interpret these anomalies to represent enhanced epikarst in the fault footwall. Our case study clearly demonstrates that a staged approach involving a progression of methods beginning with a reconnaissance VLF survey, followed by high-resolution gravity and electrical resistivity surveys, can be used to characterize a fault and fault-related karst in an area of poor bedrock surface exposure.

INTRODUCTION

Large-scale structural discontinuities in humid karst terrains are notoriously difficult to locate and characterize due to poor bedrock exposures, low topographic relief and well-developed residual soils. Recognizing that faults can localize and enhance karst features, we used geophysical methods to detect karst and bedrock discontinuities in an effort to add needed resolution to a widely recognized, but only approximately located regional fault. We integrated several shallow geophysical methods with complementary strengths to better constrain the attitude and position of a regional fault and related karst. The sequence of application of these methods was carefully chosen to optimize detection of the buried fault over a broad area. This sequential approach can be applied to other karstified faulted terrains.

The Valley and Ridge Province of the Central Appalachians consists of folded and faulted Paleozoic strata, deformed during the Permian Alleghanian orogeny and subsequently deeply eroded (Faill, 1998). Our study area lies within the karstified Nippenose Valley, formed in the hinge of the first–order, breeched Nittany Anticlinorium (Figure 1). The floor of the valley is underlain by gently dipping Middle to Upper Ordovician carbonate rocks transected by the St. James Fault Complex on the west end of the valley, the focus

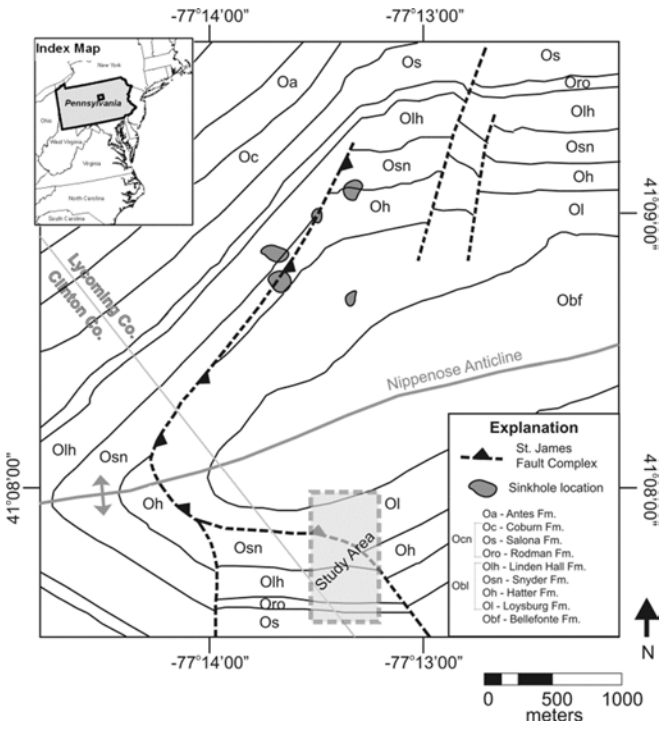

Figure 1. The study area (shaded area) is located in north-central Pennsylvania (index map) at the southern extent of the St. James Fault complex in Nippenose Valley (after Faill and Wells, 1977; Lloyd and Carswell, 1981). The fault complex crosses the hinge of a major anticline, is unexposed, and is only approximately located. The Bellefonte Formation (Obf) is dominated by dolomites. The Loysburg Formation to Linden Hall Formation stratigraphic interval (Obl) and the Rodman Formation to Coburn Formation stratigraphic interval (Ocn) are dominated by limestones.

of this case study (Faill and Wells, 1977; Lloyd and Carswell, 1981). The center of Nippenose Valley is underlain by the dolomitic Bellefonte Formation of Ordovician age, and limestone dominates the other Ordovician carbonate rocks on the flanks of the valley. The St James fault trace is curved and concave to the east, is at least 10 km long, and branches into two splays at its southern extent. The curvature of the map trace suggests that the fault predates the development of the Nittany Anticlinorium. The position and shape of the fault trace is approximated based upon limited bedrock exposures in sinkholes, quarries and bedrock pinnacles that require a fault to account for offset contacts. Although offset formation contacts across the fold are best explained by faulting, the fault is not exposed and its precise location and dip direction are uncertain (Faill and Wells, 1977; Lloyd and Carswell, 1981). Published maps indicate the St. James Fault is an approximately located thrust fault that dips toward the north or east (toward the center of the valley). However, it is possible to produce the same map pattern using a west or south dipping normal fault geometry. Determining the dip direction and location of the fault are essential for understanding likely zones for potentially hazardous sinkhole development.

The lower Paleozoic carbonates of the Appalachians are renowned for karst features and have been a focus for numerous geophysical studies on shallow karst features (e.g. Nyquist et al., 2007; Hiltunen and Cramer, 2008; White and White, 2009). Structural discontinuities such as faults, fractures, and veins play a role in localizing and accelerating karstification (White, 1988). In the Nippenose Valley, the shape and orientation of sinkholes are related to the fracture pattern in the carbonate bedrock (Miller, 1995). The northern portion of the St. James Fault trace appears to correspond with isolated sinkholes (Figure 1). Published geologic maps provide the approximate location and strike of the fault, however, the exact location and orientation of the fault is not resolved.

In order to establish a more precise fault trace location and to potentially determine the dip angle, we applied multiple geophysical methods within the focused study area (Figure 1). The study area presents an ideal location to apply geophysics to non-invasively characterize the St James Fault for two important reasons. First, the dolomitic Bellefonte Formation (Obf) is closest to the ground surface north of the St. James Fault trace and may be as much as 0.2 g/cm^3 greater than the density of the overlying limestone formations (Obl). And second, based on map and stratigraphic relations, the maximum throw (76 m) along the fault trace within Nipponese Valley occurs within the study area. The study area is also characterized by ground surface elevation ranging from 235 to 255 m above sea level (ASL), and water table elevation of 204 m ASL (Lloyd and Carswell, 1981).

The combined and sequential use of electromagnetic, gravity, and electrical resistivity methods provided the necessary data to hone in on subsurface anomalies related to the fault and interpret the subsurface structure at the study area. We are able to more precisely locate the fault south of the previous mapped location and establish the dip direction of the fault. Further, using integrated geophysical results, we are able to confirm that the St James Fault has reverse dip separation. Finally we are able to detect a distinct difference in karstification across the fault trace that corresponds with differences in lithology.

METHODS

Geophysical Data Locations – GPS positioning

The latitude, longitude, and elevation of all of the geophysical data stations were determined using a real-time kinematic global positioning system (RTK-GPS) consisting of two GPS antennas, a base and rover. The base GPS antenna logged position information on three different days for a total of 12.5 hrs. These data files were post-processed using the online positioning user service (OPUS) from the National Geodetic Survey (NGS.NOAA.gov) to provide the location of the base station. The accuracy of the base station location was evaluated by comparing the three OPUS solutions from different days in addition to precision associated with each OPUS solution to the latitude and longitude relative to NAD83 (CORS96 – EPOCH:2002.0) and orthometric height relative to NAVD88 – Geoid03. The rover antenna communicated with the base antenna to determine the RTK-GPS position of the geophysical data relative to the base station. The precision of the RTK-GPS measurements (from the rover) were calculated

internally based on the dilution of precision (DOP) and averaging a minimum of five observations of position.

Very low frequency (VLF) electromagnetics (EM)

The VLF method uses EM signals between 15 and 30 kHz broadcast dominantly by governmental transmitters for long-range communication. This method measures the orientation of the EM field above the earth's surface at VLF frequencies and traditionally is used by geophysicists to locate mineral deposits. The VLF method is also useful for detection of near-surface karst, fractures and faults as it sensitive to changes in the resistivity structure of the subsurface (Chalikakis et al., 2011). The VLF method is discussed in detail by McNeill and Labson (1991).

Significant changes in the resistivity structure of the subsurface in karst environments are controlled by the electrical properties of the subsurface material. Across strike changes in bedrock lithology may result in east-west (strike-parallel) VLF anomalies. The unaltered bedrock, limestone or dolomite, at the field site is expected to have a resistivity greater than 1000 ohm-m (Knight and Endes, 2005). Altered bedrock, residual soil and clay plugs are expected to have resistivity less than 100 ohm-m (Knight and Endes, 2005), however, decreased water content would cause the resistivity of these materials to increase. Any air-filled voids, if present, would also increase the bulk resistivity of the subsurface. Other than voids, the primary factor that we anticipate to govern the resistivity of the subsurface is the thickness of the clayey soil / weathered bedrock, which ranges between <1 m thick to >20 m thick in quarries within the Nippenose Valley.

We used a Wadi VLF system (ABEM Instruments) as a reconnaissance tool to potentially locate karst related to the St. James Fault and/or locate the fault itself. The Wadi VLF system measures the real (in-phase) and imaginary (quadrature) components of the magnetic field as the ratio between the vertical field and the horizontal field. The NLM transmitter (LaMoure, N.D., USA) at 25.2 kHz was selected for the three approximately 650 m long north-south VLF profiles (Figure 2) chosen to be approximately perpendicular to the mapped fault trace. Each profile line consisted of approximately 87 stations spaced 8 (±0.5) m apart (Figures 2 & 3). We assessed the error associated with each VLF observations by collecting repeat measurements at a single station. The VLF results will show an increase or decrease in raw (in-phase and quadrature) values depending on the resistivity structure of the subsurface. The inflection point between low and high raw values should approximately overly the transition between resistive and conductive subsurface material (Karous and Hjelt, 1983). The in-phase component is sensitive to very conductive material such as the clayey soil. While the quadrature component is sensitive to smaller changes in material conductivity, such as fresh-water saturated fault zone. An increase in the depth of the conductive material increases the width of the in-phase and quadrature responses.

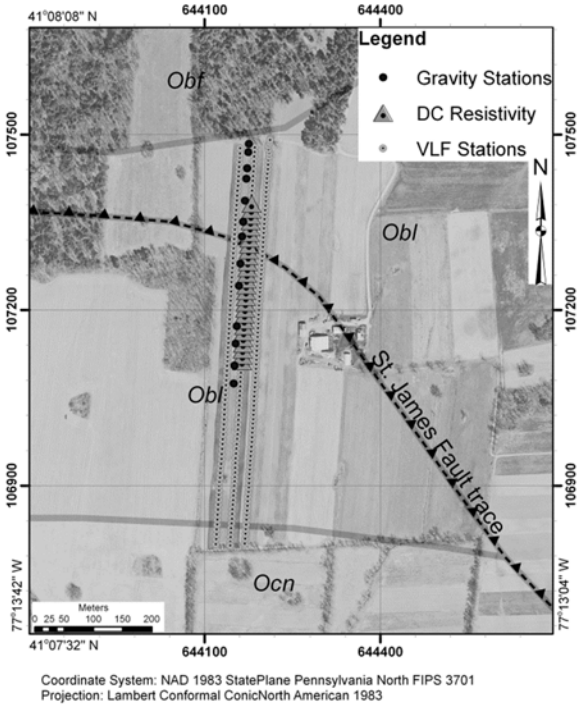

Figure 2. The study area, an agricultural field, and expected geologic contact locations with mapped fault trace location (PAGS, 2001). The geophysical data were collected over an area of 3.35 x 104 m2 with no surface expression of the fault. Refer to Figure 1 for stratigraphic symbols and descriptions. Survey locations for VLF, ERI and gravity are shown on the map. 300 m grid lines in both Northing and Easting according to Pennsylvania State Plane North are displayed.

The in-phase and quadrature components at the VLF stations were then spatially filtered individually to calculate the respective current density (Karous and Hjelt, 1983). The filtered data were calculated at increasing intervals between 8 m and 56 m, in 8 m increments, to provide the in-phase and quadrature

current density pseudo-sections, respectively. The same filter coefficients shown in Karous and Hjelt (1983) were used for our processing. The in-phase current density data will exhibit a local maximum above the more conductive material (Karous and Hjelt, 1983). The OPUS-corrected RTK-GPS station positions and the measured data from the VLF instrument were combined during post-processing.

Gravity

Subsurface features such as changes in bedrock lithology or fault-offsets in bedrock can lead to detectable differences in relative gravity readings. Telford et al. (1990) shows that simple shapes, such as "slabs" (parallelograms or rectangles in cross-section), which have a density contrast compared to the material located below a horizontal contact with the slab or adjacent to the slab across an angled contact, may be used to interpret gravity anomaly observations. Further details about the gravity method may be found in most introductory applied geophysical textbooks (e.g., Telford et al., 1990; Keary et al., 2002; Burger et al., 2006; Milsom and Eriksen, 2011). The dip direction can be inferred from the location and shape of gravity anomalies relative to the fault trace. A north-dipping reverse fault should produce a gravity high north of the fault trace due to repetition of the dolomite in the hanging wall (Saltus and Blakely, 2011). In contrast, a south-dipping normal fault produces a gravity plateau north of the fault trace due to the proximity of the dolomite in the footwall. Additionally, an observable change in gravity is expected if the limestone formations (Obl) have a greater amount of weathering in comparison to the dolomitic formations (Obf) since the clayey soil would be at least 0.2 g/cm^3 less dense than the intact bedrock. Thus, we used the gravity method to identify and model changes due to the bedrock juxtaposition across the St James fault and possible fault-related karst. The VLF data should provide a general location of the fault and thus reduce the amount of gravity data needed to locate the fault position.

We used a self-leveling, automatic Lacoste & Romberg Graviton-EG gravimeter. The sensitivity of our gravimeter was determined by collecting 18,216 observations recorded digitally every 2 sec continuously during a 10 hour and 8 minute period and comparing to expected changes in gravity due to tidal fluctuations. The observations were averaged over a 4 min time range, and Table 1 presents the relative frequency analysis of the differences between the average gravity measurement and the expected gravity value from tidal predictions (Micro-g Lacoste, 2007). The frequency table indicates that 99% of the 4 min average measurements are less than ±0.01 mGal different from the expected tidal measurement. The sample standard deviation, calculated from the difference between the 4-min average and the individual 2-sec measurements, as well as the 95% confidence interval on the average are also presented in Table 1. Comparing the results of the frequency analysis to both the standard deviation and the 95 % confidence interval, it is clear that the 95% confidence interval better describes the precision for each average gravity measurement. These data indicate that we need to average four minutes of gravity measurements from a gravity station to achieve the anticipated ±0.01 mGal precision.

Table 1. Accuracy check for gravimeter (Lacoste & Rhomberg Gravitron-EG) used for study. 18,216 measurements recorded digitally every 2 sec continuously over a 10 hour and 8 minute period. Frequency analysis based on calculated deviations between 4 minute running averages of observations and the theoretical tide value (Micro-g Lacoste, 2007). Standard deviation based on the variance between the observations and the theoretical tide-value. The 95% confidence limit on the average calculated using Student's T test. The similar result between 95% confidence limit values and cumulative percent of deviations within the confidence limit indicate that the 95% confidence should be used to indicate precision of the observations.

	4 min running average	
Bin (mGal)	# in Bin	Cumulative %
≤ 0.001	10370	57.1%
≤ 0.005	4995	84.6%
≤ 0.01	2615	99.0%
≤ 0.05	190	100.0%
Sample standard deviation based on the data		
	0.041 mGal	
95% confidence limit of average		
	0.007 mGal	

We chose a 420 m long gravity survey profile based on the results of the VLF survey (Figures 2 & 3). It crosses the published mapped location of the fault trace

238 m north of initial gravity station. The gravimeter collected continuous measurements (~30 readings/minute) for greater than 4 minutes at every gravity station. The gravity stations were spaced between 15 m and 69 m apart, with most stations being separated by 30 (±5) m, with changes in station spacing due to surface vegetation – farmer's corn crop. During data collection, the instrument operator moved 25 m away from the gravimeter to avoid any effect caused by the proximity of the operator to the instrument. The mean gravity measurement is calculated at each station from the four plus minutes of gravity observations and the 95% confidence interval on the mean gravity is calculated. Repeated base station gravity measurements every two hours during the survey period provided necessary information to remove any drift in the gravimeter from each station observation along the profile. The latitude, longitude, and elevation for each of the 13 gravity stations were determined using OPUS-corrected RTK-GPS measurements. The station locations were used for the tidal correction and topographic corrections (free-air, Bouguer and terrain). The PA state 1-m digital elevation model (DEM) derived from airborne LiDAR measurements (PAMAP, 2006) provided the regional (down sampled to a 30 m DEM) and local input to calculate the terrain correction at each gravity station.

Electrical resistivity imaging (ERI)

This method was used to confirm the results of the VLF survey and ultimately, provide information necessary for analyzing the gravity data, specifically the thickness of the clayey soil. ERI directly applies an electrical current to the ground and measures the voltage to calculate the subsurface resistivity. Using a multi-electrode system, profile and sounding measurements are collected during one deployment, generating a resistivity pseudo-section along the resistivity line (Figures 2 & 3). The resistivity line was positioned in the northern portion of the middle VLF survey line based on promising gravity observations in that area. The ERI method is described in detail in introductory applied geophysical textbooks (e.g., Telford et al., 1990; Keary et al., 2002; Zonge et al., 2005; Burger et al., 2006; Milsom and Eriksen, 2011). Roth et al. (2002) successfully demonstrates that the multi-electrode ERI method is capable of locating subsurface voids and delineating the vertical extent of epikarst in southeastern Pennsylvania.

We used a Sting R1 with 28-channel Swift automatic electrode switching box (AGI, Inc) to collect a 270 m Wenner ERI line with a minimum a-spacing of 10 m and a maximum a-spacing of 90 m to acquire the apparent resistivity data. The error of the apparent resistivity observations for each electrode combination is recorded automatically as the standard deviation between three repeated measurements. Observations with greater than 1% standard deviation were excluded from inversion. The apparent resistivity data were combined with the OPUS-corrected RTK-GPS elevations of each electrode and inverted to determine the resistivity model of the subsurface using EarthImager 2D (AGI, Inc.). In addition, the sensitivity of the resistivity model to the starting resistivity model is calculated by EarthImager 2D and indicates the depth to which the subsurface resistivity structure is well constrained by the observations.

RESULTS

RTK-GPS Position Accuracy and Precision

The OPUS solution for the latitude and longitude of the RTK-GPS base station had a calculated precision of 0.001 m and 0.007 m, respectively. The three solutions for the position of the base station in Pennsylvania State Plane North (3701 PA N) from three different dates of base logging agreed with each other to 0.009 m in northing and 0.008 m in easting. The OPUS solution for the orthometric height (elevation) of the RTK-GPS base station had a calculated precision of 0.013 m. The three solutions for the elevation of the base station agreed with each other to 0.012 m. Hence, our GPS positioning is considered to be accurate to within 0.009 m in latitude (or northing) and longitude (or easting), and 0.013 m in elevation.

The RTK-GPS measurement precisions for all VLF stations were ≤0.01 m in the horizontal plane and ≤0.015 m in the vertical direction. The RTK-GPS measurements for the gravity stations and ERI electrode locations were more precise due to the increased distance to tall trees. The median precision for all gravity stations was 0.004 m (ranging from 0.003 to 0.009 m) in the horizontal plane and 0.007 m (ranging from 0.006 to 0.013 m) in the vertical direction.

VLF

The VLF results reveal both in-phase and quadrature anomalies when gridded using a minimum curvature interpolation method with eight meter cell size (Figure 3). Repeated measurements at the south-western most station yielded an estimate of error in the VLF measurements to be ±0.1% for both in-phase and quadrature components. The in-phase data indicate several transitions from high to low values extending across the survey grid with the most rapid transitions at approximately 107100 m and 107400 m north (Figure 3a). The quadrature data (Figure 3b) indicate two rapid transition zones from high to low values extending across the survey grid at approximately 107130 m and 107300 m north. Interestingly, the VLF anomaly orientations north of the mapped fault trace (approx. 107300 m north) are sub-parallel to the mapped fault trace, whereas south of the mapped fault trace, the VLF anomalies are sub-parallel to the geologic formation contacts (for example Obl-Ocn in Figure 3). The location and orientation of these in-phase and quadrature anomalies warranted further investigation using the gravity method.

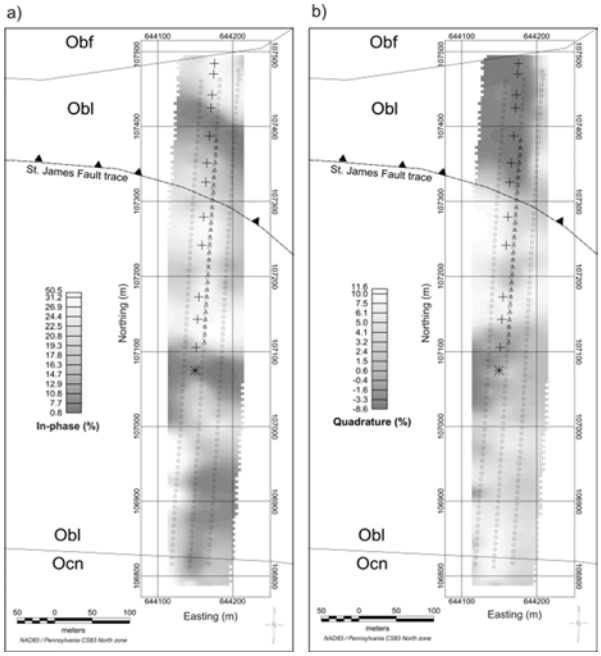

Figure 3. Geologic map overlain with raw VLF observations (represented by open circles) used with a minimum curvature interpolation to produce the gray-scale in-phase (a) and quadrature (b) component images. The maps illustrate predominantly east-west trending anomalies subparallel to formation contacts south of 107200 m north. The anomaly trending AZ 310˚ in the northern portion of the study area is subparallel to the mapped trace of the St. James Fault. Survey locations for ERI (Δ) and gravity (+) are shown on the map. The zero position on the gravity profile corresponds with the southernmost gravity station (✳).

In-phase and quadrature current density pseudosections for the middle VLF profile in Figure 3 were calculated to provide depth information (Figure 4). The ground surface elevation for each VLF station minus the filter length (8, 16, 24, 32, 40, 48, and 56 m) is used to display the depth axis for the psudeosections, however, the psuedosections do not show the true current distribution with respect to depth in the subsurface (Fraser, 1981). The in-phase current density data indicate four positive anomalies at approximately 106940 m, 107110 m, 107230 m, and 107420 m north (Figure 4a). The current density from the quadrature component indicates three positive anomalies at approximately 107140 m, 107230 m, and 107360 m north (Figure 4b). The increased in-phase and quadrature current density zones do not correspond to the mapped fault trace.

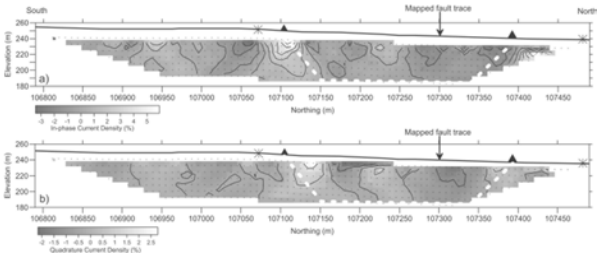

Figure 4. Current density pseudosections calculated from the in-phase (a) and quadrature (b) components of the VLF survey. Horizontal distance is expressed in northings for each VLF station and the ground surface elevation for each VLF station minus the filter length (8, 16, 24, 32, 40, 48, and 56 m) is used for the y-axis to display the pseudosections. Beginning and ending position for the gravity (✳) and ERI (▲) surveys are shown on the pseudosections. The white dashed line on each pseudosection represents the extent of the ERI model.

Gravity

The location of the gravity profile was chosen based on the VLF results. It is 10 m west of the middle of the three VLF transects and was positioned to cross the most significant VLF anomalies. The initial gravity station is located at 107070 m north and we refer to the other gravity stations with respect to their distance relative to this location. The mean tide and drift corrected gravity measurements as well as the station elevations are shown in Figure 5a. We achieved <0.01 mGal precision on each measurement. The 95%

confidence interval is not visible at the scale of the figure. In order to correct the gravity measurements for topographic effects, Nettleton's (1976) approach was used to determine the correct reduction density. This approach provided a minimum density of 2.5 g/cm^3 to decouple the corrected gravity measurements from the surface topography. On the other-hand, a reduction density greater than 2.9 g/cm^3 results in a negative correlation between corrected gravity measurements and surface topography. Hence, we used an average crustal density of 2.67 g/cm^3 to reduce the observed mean gravity data to Bouguer gravity anomaly data.

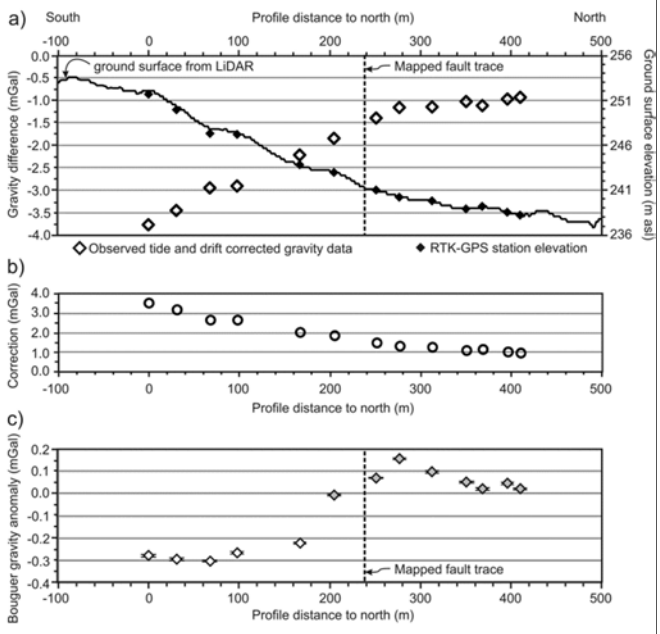

Figure 5. (a) Tide and drift corrected, 4 min averaged, gravity observations. Elevations determined from both RTK-GPS at time of gravity survey and 1 m DEM collected by aerial LiDAR (PAMAP, 2006). (b) Combined Free Air, Bouguer, and terrain corrections for each station. (c) Corrected gravity measurements at each gravity station. The gravity profile north of 200 m (gray diamonds) is consistent with a standard faulted slab gravity effect (Telford et al., 1990).

Figure 5b shows the combined topographic correction applied to each station, which combines the Free Air, Bouguer and Terrain corrections using a 2.67 g/cm^3 reduction density. Given that the gravity profile (Figure 5c) has negligible regional gradient, it appears that our Bouguer gravity data are not sensitive to the gentle southward dip of the Bellefonte strata. However, the Bouguer gravity anomaly data (Figure 5c) clearly indicate an increase in the average density at approximately 180 m along the profile. In addition, the 8 data points north of 200 m (Figure 5c) appear to have a similar anomaly shape as would be expected from a faulted slab model (Telford et al., 1990). In order to better characterize the fault dip and location, we collected ERI data to provide further constraints on the gravity data. We further discuss gravity findings in the Integrated Results section.

ERI

The ERI location was selected to provide confirmation of the gravity data (Figure 3). The results from the ERI (Figure 6) corroborate the VLF findings and provide the thickness of the conductive materials. The

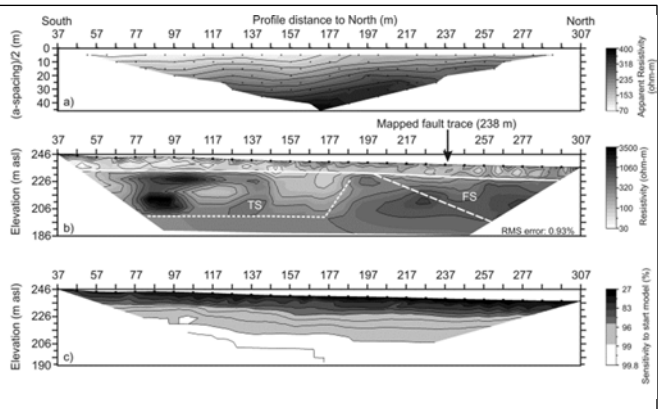

Figure 6. (a) Apparent resistivity observations from a Wenner profile using a 10 m electrode spacing centered on increase in Bouguer anomaly data from Figure 5. The position locations are relative to gravity profile. (b) Resistivity model inverted from observations with a global RMS error of 0.93% between predicted apparent resistivity from model and the observations. The increased thickness of the conductive material south of 190 m coincides with stronger current density in VLF shown in Figure 4 south of 107260 N. The 13 m depth to resistive material across most of the resistivity profile (solid white line) is used in the gravity inversion. The location of the truncated slab (TS) and faulted slab (FS) from the gravity inversion are outlined with short- and long-dashed white lines, respectively. (c) Sensitivity analysis relative to starting resistivity model. Greater sensitivity indicates that the ERI observations poorly constrain those portions of the final resistivity model in (b).

resistivity model of the subsurface indicates a significant change in thickness of the conductive material at a position of 187 m on the profile. Interestingly, this agrees with the Bouguer gravity data, where the mass of the subsurface increases (due to a change in either density and/or thickness) at the same location on the profile. North of 187 m, the conductive material is 13 m thick, while south of this position it appears to be as much as 40 m thick. A 13 m thick layer of conductive material extends along the entire profile.

This shallow cover of conductive material limits the depth of investigation. The confidence in the resistivity model (Figure 6b) is defined by the model sensitivity (Figure 6c). The inverse resistivity model is greater than 99% sensitive to the starting model used for the resistivity inversion at increasing depths below grade along the profile (Figure 6c). The minimum depth is 24 m below grade, while the maximum depth is 35 m below grade near the mapped fault trace position. Thus, the resistivity results should be viewed as approximate at best below these depths.

Integrated Model

The increased thickness of the conductive material south of the mapped fault trace in the ERI data can be explained by a truncated slab exhibiting a density contrast in the subsurface (Figure 7a). The VLF data indicates that this feature extends >25 m perpendicular to the gravity line, thus we assume the slab has infinite strike length (i.e. the truncated slab extends east-west sufficiently far to be considered infinite within the study area) allowing for use of straight-forward inverse modeling. We further calculate the gravity effect of an infinite strike length faulted slab (Figure 7b). These two gravity effects are used to invert the gravity data to determine the fault trace location on the profile line and the dip direction in order to achieve our project goals. Fully unconstrained inversion is not attempted due to the non-linear nature of the gravity effects. We do not expect to resolve the truncation angle of the slab as it does not produce a resolvable gravity effect (Telford et al., 1990), however, we do expect to resolve the dip direction (Saltus and Blakely, 2011).

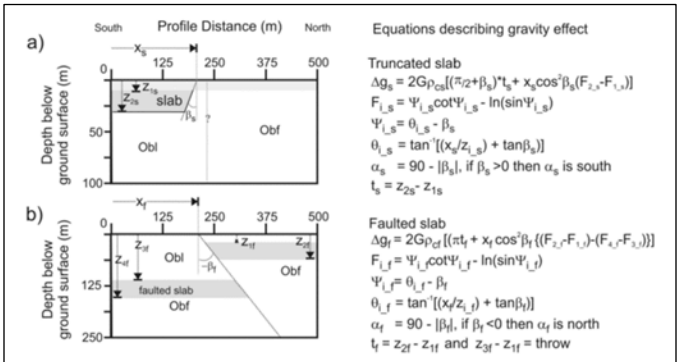

Figure 7. (a) Truncated slab model after Telford et al. (1990) and equation describing gravity effect (Δg_s) due to the truncated slab model, where G is 6.67 x 10^{-11} N $(m/kg)^2$, ρ_{cs} is the density contrast between truncated slab and nearby material, t_s is the thickness of the truncated slab, x_s is trace of the truncation plane, α_s is truncation dip angle which possesses dip direction and z_{i_s} is the depth to locations on the slab where i is either 1 or 2. (b) Faulted slab model after Telford et al. (1990) and equation describing the gravity effect (Δg_f) due to the faulted slab model, where ρ_{cf} is the density contrast between faulted slab and surrounding material, t_f is the thickness of the faulted slab, x_f is location of the fault trace, α_f is fault dip angle which possesses dip direction and z_{i_f} is the depth to locations on the slabs where i is either 1, 2, 3 or 4.

The Bouguer gravity anomaly data north of 200m (Figure 5c) are inverted by constraining the faulted slab properties using a 76 m fault throw, based on mapped stratigraphic separation, (Faill and Wells, 1977; Lloyd and Carswell, 1981) and a depth of 13 m to the top of the faulted slab (Z_{1f}), based on the ERI data. In addition, we constrain the density contrast (ρ_{cf}) to be less than 0.2 g/cm^3, the maximum difference between average limestone and average dolomite. Limiting ρ_{cf} effectively constrains the thickness of the faulted slab (t_f). We performed a gridded search procedure to locate the least-mean square (LMS) error between the unconstrained variables ($0<X_f<400$ m and 5^o north $<\alpha_f>5^o$ south, or $-85<\beta<85$) in the gravity effect predicted by the faulted slab model (Figure 7b) and the Bouguer gravity anomaly data north of 200 m (Figure 5c). The result of the constrained inversion has a root-mean square (RMS) misfit of 1.1% between the eight observations and predicted gravity effect from the faulted slab model properties in Table 2 (Figure 8a). An

Table 2. Results of gravity inversion for the faulted slab model and truncated slab model. * Model properties constrained by expected fault properties from geologic map. ** Model properties constrained by ERI results. *** Model properties constrained by average material properties.

Faulted Slab Inversion Results		Truncated Slab Inversion Results	
Heave*	76 m		
Z_{1f} **	13 m	Z_{1s} **	13 m
α_f	34 degrees to north	α_s	70 degrees to south
X_f	185 m	X_s	191 m
ρ_{cf}***	0.2 g/cm^3	ρ_{cs}***	0.2 g/cm^3
t_f	30 m	t_s	34 m

RMS error of 0.9% is possible by releasing the ρ_{cf} constraint on the solution, with a ρ_{cf} of 0.39 g/cm^3 and t_f of 17 m. Exploring the resolution of the inversion results, we note that the RMS error increases to 1.2% for values of ρ_{cf} less than 0.18 g/cm^3 and t_f 33 m, which we associate with the inherent non-uniqueness of the problem. More important to our study, the RMS error increases to 1.2% for values of X_f greater than ±10 m from the value in Table 2. Further, RMS errors greater than 1.2% result from a ±5 degree change in α_f. Although we consider the α_f as poorly determined (Telford et al., 1990), we note that the LMS solution agrees with typical dip angle of a thrust fault and that the dip direction is north.

We next look to quantify the thickness of the low resistivity zone south of 187 m on the gravity profile. The predicted gravity anomaly for the faulted slab model (Figure 8a) at each position is subtracted from the observations to determine the residual anomaly (Figure 8b). These residual gravity anomaly data are inverted to determine the truncated slab properties. We use a 13m depth to the truncated slab (Z_{1s}) based on the ERI data, and constrain the ρ_{cs} to be less than 0.2 g/cm^3. A similar gridded search procedure located the LMS error between the unconstrained variables (X_s and α_s) in the gravity effect predicted by a truncated slab model (Figure 7a) and the residual gravity anomaly data. The resulting truncated slab model properties (Table 2) fit the residual gravity anomaly data with a RMS error of 0.9% (Figure 8b). An RMS error of 0.8% is possible by releasing the ρ_{cf} constraint on the solution, with a ρ_{cs} of 0.53 g/cm^3 and t_s of 12 m. Exploring the resolution of the inversion process, the RMS error increases to 1.0% for values of the slab cutoff (X_s) less than 140 and greater than 220 m, this indicates that the resolution of X_s from the gravity data is poor. The truncation angle (α_s) from the gravity data is poorly constrained as indicated by Telford et al. (1990). Specifically the RMS error increases to 1.0% for values of α_s less than 30^o south and greater than 30^o north, thus over 120^o of uncertainty. However, the ERI data (Figure 6) indicate that the X_s for the truncated slab (TS), the edge of the conductive material, is located at approximately 190 m and dips south at approximately 70 degrees.

We accept the values for the variables in Table 2 for fitting the combined geologic, gravity, and ERI data. We then compare the combined predicted gravity effect of the faulted and truncated slabs using these model values with the Bouguer gravity anomaly data, and determine that our combined model has a RMS misfit of 1.0% (Figure 8c). Ultimately, we construct a shallow geologic cross-section based on the results of the combined data inversion (Figure 8d).

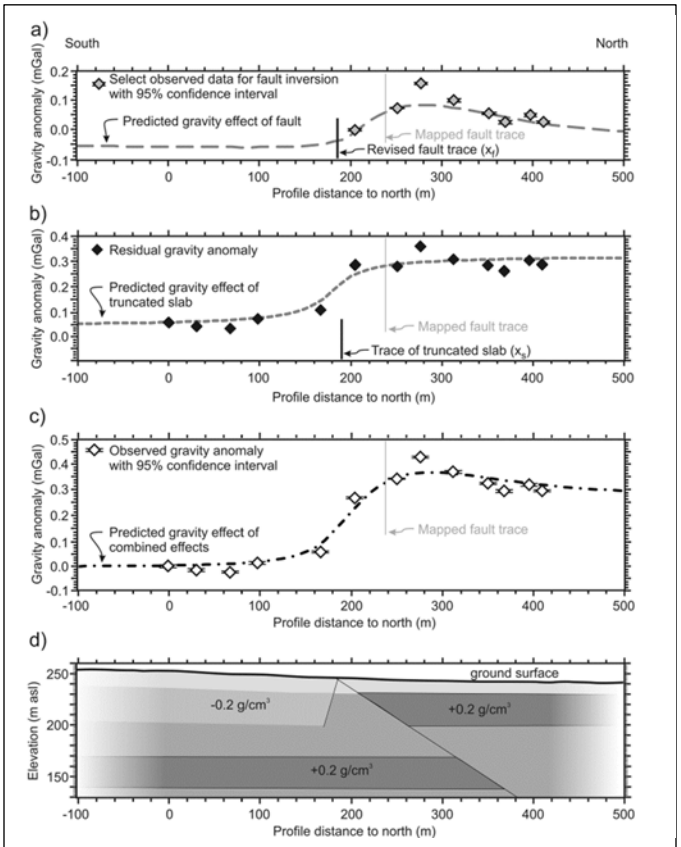

Figure 8. (a) Observed gravity data north of 200m along profile and predicted gravity effect of the LMS fit for a faulted slab model with a 1.1% RMS error. (b) Residual gravity anomaly after subtracting the predicted gravity effect in (a) from the observations. The predicted gravity effect for the truncated slab model fits these data with a RMS error of 0.8%. (c) Combined predicted gravity effect (faulted slab and truncated slab models) fit the observed gravity anomaly with a 1.0% RMS error. (d) The geologic cross-section based on combined resistivity and gravity data inversions constrained by the expected throw and ρ_c. The upper approximately 13 m of the subsurface is characterized by conductive material (clay) and is dominantly uniform across the profile.

DISCUSSION

The results of our integrated geophysical study indicate that the position of the St. James Fault trace (185 m on the gravity profile) is 53 m south of the currently mapped position (238 m) from Faill and Wells

(1977) and Lloyd and Carswell (1981). The dip direction of the St. James Fault was not previously known. The gravity data are consistent with a north-dipping thrust fault interpretation for this segment of the fault.

The gravity data and ERI model reveal a significant change in the subsurface at 191 m on the profile, which corresponds to a VLF current density anomaly change at 107260 m north. This indicates that the material to south of this position is conductive to greater depth and less dense. These properties suggest a thicker, weathered zone consisting of clayey material located south of 191 m. Interestingly, the location of this transition corresponds closely with our proposed fault location (185 m on the profile). Additionally, the limestone-dominated bedrock in the footwall of the fault may explain increased weathering in the footwall; whereas the hanging-wall is dominated by more weathering-resistant dolomite.

The ERI model indicates an anomalous zone between 80 and 110 m and 15-40 m depth exhibiting resistivities greater than 3000 ohm-m, which may be related to a subsurface void. As the gravity data do not indicate a mass deficit at the nearest gravity station 10 m away, this feature is interpreted to have small dimensions.

While the VLF and ERI results generally agree with each other and were useful in this study, neither is sensitive to the St. James Fault plane. Rather, they are sensitive to bedrock, karst and surficial geology changes that occur across the fault contact. There is not a gravity anomaly (at 328 m on the profile) located in the same position as the VLF in-phase anomaly at 107400 N (Figure 3). We interpret the change in strike of the VLF anomalies to be representative of the hanging wall.

We recognize that while the assumption of infinite strike length may be reasonable for the fault model, this assumption is less realistic for the truncated slab of clay due to the effect of localized accelerated weathering. The scope of this project was limited in aerial extent. Future work may be directed to better constrain the strike-length of the features to allow for three-dimensional modeling. In addition, further geologic observations that determine the density contrast between the clay, limestone and dolomite would add further resolution to the model.

CONCLUSION

Our case study of a buried fault capitalized on the strengths of multiple geophysical methods to pin down the location of the fault trace, its orientation and related karst. VLF was useful as a reconnaissance tool to refine our search for the buried fault trace. ERI helped to define karst that had different expression in the footwall and hanging wall of the fault. Gravity was most effective at constraining the location and orientation of the fault plane. Our combined results indicate that the fault trace should be adjusted 53 m southward (77^{o} 13’ 26.67” W / 41^{o} 7’ 52.56” N) of its current mapped position (Faill and Wells, 1977) in our study area. The results support the interpretation that the St James fault is a north-dipping reverse fault. Our results are most consistent with a shallowly dipping fault (34˚). Karst is most pronounced in the footwall of the St James fault, perhaps as a result of the predominance of limestones in that stratigraphy and/or as a result of footwall deformation. The modified fault trace location may be used to focus karst related studies, looking for future hazards associated with potential sinkhole development in the area. This successful case study of the St. James Fault provides incentive to use similar combined methods to investigate other buried faults in karstified terrains.

ACKNOWLEDGEMENTS

This project is an outgrowth of undergraduate research by Byler that was funded by a McKenna Environmental Research Fellowship and the Marchand Fund of the Bucknell University Geology Department. Access to private properties in Nippenose Valley is gratefully acknowledged. We thank Jon Algeo, Xavier Hope and Dennis Lee, for providing field assistance. We appreciate the comments from three anonymous reviewers and Associate Editor Dr. David Nobes.

REFERENCES

Burger, H. R., A. F. Sheehan, and C. H. Jones, 2006, Introduction to applied geophysics: Exploring the shallow subsurface: W.W. Norton.

Chalikakis, K., V. Plagnes, R. Guerin, R. Valois, and F. Bosch, F., 2011, Contribution of geophysical methods to karst-system exploration: an overview: Hydrogeology Journal **19**, 1169–1180.

Faill, R.T., 1998, The geologic history of the north-central Appalachians; Part 3, The Alleghany Orogeny: American Journal of Science, **298**, 131-179.

Faill, R. T., and R. B. Wells, 1977, Bedrock geology and mineral resources of the Linden and Williamsport quadrangles, Lycoming County, Pennsylvania: Pennsylvania Geological Survey Atlas 134ab.

Hiltunen, D. and B. Cramer. 2008, Application of seismic refraction tomography in karst terrain: Journal of Geotechnical and Geoenvironmental Engineering, **134**, 938–948.

Karous, M., and S. E. Hjelt, 1983, Linear filtering of VLF dip-angle measurements: Geophysical Prospecting, **31**, 782-794.

Keary, P., M. Brooks, and I. Hill, 2002, An introduction to geophysical exploration: 3rd edition, Blackwell.

Knight, R. J., and A. L. Endres, 2005, An introduction to rock physics for near-surface applications, *in* D. Butler, ed., Near-surface geophysics, vol. 1, concepts and fundamentals: Society of Exploration Geophysics, 31-70.

Lloyd, Jr. O. B. and L. D. Carswell, 1981, Groundwater resources of the Williamsport region, Lycoming County, Pennsylvania: Pennsylvania Geologic Survey Water Resources Report W51.

McNeill, J. D. and V.F. Labson, 1991, Geological Mapping using VLF radiofields, *in* M.C. Nabighian, ed., Geotechnical and Environmental Geophysics, vol. 1, Review and Tutorial: Society of Exploration Geophysicists, 191-218.

Micro-g Lacoste, 2007, Graviton-EG instrument manual.

Miller, J. H., 1995, Structural Controls on karstification in the Nippenose Valley, Pennsylvania: Undergraduate thesis, Bucknell University.

Milsom, J.J. and A. Eriksen, 2011, Field geophysics: John Wiley & Sons.

Nettleton, L. L., 1976, Gravity and magnetics in oil prospecting: McGraw-Hill Book Co.

Nyquist, J.E., J.S. Peake and M. J. S. Roth, 2007, Comparison of an optimized resistivity array with dipole-dipole soundings in karst terrain: Geophysics, 72, F139-F144

PAMAP, 2006, PAMAP Program 1 m Digital Elevation Model of Pennsylvania, PAMAP Program, PA Department of Conservation and Natural Resources, Bureau of Topographic and Geologic Survey, http://www.pasda.psu.edu, accessed 1/2012

PAGS, 2001, Bedrock Geology of Pennsylvania from Pennsylvania Bureau of Topographic and Geologic Survey, Department of Conservation and Natural Resources, http://www.pasda.psu.edu, accessed 1/2012

Roth, M.J.S., J.R Mackey, C Mackey, and J.E Nyquist, 2002, A case study of the reliability of multielectrode earth resistivity testing for geotechnical investigations in karst terrains: Engineering Geology, **65**, 225-232.

Saltus, R. W., and R. J. Blakely, 2011, Unique geologic insights from “non-unique” gravity and magnetic interpretation: GSA Today, **21**, 4-11.

Telford, W.M., L.P. Geldart, and R.E. Sheriff, 1990, Applied geophysics: Cambridge University Press.

White, W.B., 1988, Geomorphology and Hydrology of Karst Terrains: Oxford Univ. Press.

White, W. B. and E.L. White, 2009, Karst field trips; the Appalachian valleys of central Pennsylvania: Karst Waters Institute Special Publication, **15**, 10-42.

Zonge, K., J. Wynn and S. Urquhart, 2005, Resistivity, induced polarization, and complex resistivity, *in* D. Butler, ed., Near-surface geophysics, vol. 1, concepts and fundamentals: Society of Exploration Geophysics, 265-299.